Robotica (2016) volume 34, pp. 243–257. © Cambridge University Press 2014
doi:10.1017/S0263574714001404

A concept of laser scanner designed to realize 3D obstacle avoidance for a fixed-wing UAV

Cezary Kownacki*

Faculty of Mechanical Engineering, Bialystok University of Technology, ul. Wiejska 45C, 15-351 Bialystok, Poland

(Accepted May 2, 2014. First published online: June 9, 2014)

SUMMARY

This paper presents a concept of a laser scanner framework designed for obstacle avoidance used on mini fixed-wing unmanned aerial vehicles (UAVs) flying in outdoor environments. The innovation is a conical field of view that guarantees tri-dimensional (3D) obstacle detection and localization at any pitch or roll angle. This advantage is very important for the case of fixed-wing UAV flights where the attitude is changing rapidly. Measurement sequences create a map that is represented by a circular grid with the center fitted to the *x*-axis of the UAV's body, lying in the plane normal to the velocity vector and projected in the front of UAV. This means that the map cells contain differences between the safety zone radius and distances acquired from area in close proximity to the flight path. Actual UAV attitude can be compensated by rotation and shift of two masks of gains that are applied to the map to determine pitch and roll commands. Results of the simulation research conducted on the designed concept are very promising, as they present a combination of lateral and vertical obstacle avoidance. Based on the experience with laser rangefinders operating on a real UAV, it can be convincingly determined that the concept of the laser scanner is able to be brought into reality.

KEYWORDS: Laser scanner; LIDAR; Unmanned aerial vehicle; Obstacle avoidance; Mapping; SLAM.

1. Introduction

Although researchers' interest in the area of unmanned aerial vehicle (UAV) is still increasing, the problem of reliable and guaranteed obstacle avoidance remains unresolved thoroughly due to weaknesses and limitations of current perception systems, which are used onboard of a mini UAV. It should be underlined, that obstacle avoidance issues refer mostly to mini and micro UAVs since typical flight mission objectives for larger UAVs exclude them from operating at low altitudes in areas covered by natural or urban obstacles. The small size and small dynamic time constants of vehicles, which are expected to be able to avoid obstacles autonomously, are main determinants for the problem difficulty level. Having a limited payload, low computational resources, and a limited power supply is not feasible to achieve solutions adequate for all possible obstacle shapes, sizes, ambient lighting, etc. So researchers are now focusing on control algorithms that use synthetic obstacles in simulations[5,9,12,19,23] or they present obstacle avoidance demonstrations with noticeable restrictions that reduce their application to simple and special cases.[8–11,15–18] These two scopes of research taken together with addition of technology improvements can result in more autonomous systems of UAVs.

Most of the examples of obstacle avoidance applications rely on vision sensors, which provide significant amounts of information about UAV surroundings without a significant increase in payload.[8–11,15,17–19,23] Although this may sound excellent, vision sensors greatly suffer from complexity of video processing algorithms, low resolution, ambient lighting, scene contrast, weather conditions, and computational resources of onboard processors, from battery capacity. Combining a vision system with other obstacle detection techniques such as sound navigation and ranging

* Corresponding author. E-mail: c.kownacki@pb.edu.pl

(SONAR) eliminates some of these issues, but the vehicle payload is also increased and additionally the overall system is more complex. Therefore, vision systems typically run under specific conditions, applied to selected vehicles or exploration cases without a variety of real-world scenarios with closed-loop control enabled. Moreover, most of vision-based avoidance systems are applied to larger hover vehicles since miniature cameras fixed to a small fixed-wing UAV is still insufficient to precisely locate objects and still requires a mechanical stabilization. An alternative to vision systems could be laser rangefinders. A few articles present successful usages of this type of sensors in outdoor flights;[16,20] but at this time one or even two laser rangefinders do not provide enough information to cover all cases of various obstacle sizes and relative locations due to the effect of the limited field of view. Hence, using a laser scanner or a light detection and ranging (LIDAR) system for outdoor obstacle avoidance purpose, especially in urban environments could be a better idea. Such LIDAR system could eliminate a majority of weaknesses of two sensors approach, and simultaneously it will merge the same possibilities, i.e. obstacle avoidance with a feature of canyon flights.

Typically laser scanners or LIDARs with simultaneous localization and mapping (SLAM) algorithms are used for two main topics described in many articles: indoor environment mapping and outdoor terrain/obstacle mapping.[2,21] The mutual property of these two wide topics is employing vertical taking off and landing vehicles (VTOL), which are capable of flying horizontally. It obviously guarantees undisturbed and stable orientation of the scanning plane that is required for two-dimensional/tri-dimensional (2D/3D) map creation. In cases of indoor mapping scanners horizontally explore an unknown environment to prepare an occupation grid and to find an optimal flight path. A different approach was presented by MIT Robust Research Group. Their fixed-wing vehicle, which won the AUVSI contest in 2012, used LIDAR to deduce the vehicle position by matching the laser scan to an already known 3D map. Hence, it was possible to avoid obstacles in indoor missions, but the remaining question is how such LIDAR odometry would work in uncertain environments? Also, in another work[1] scan-matching was used to estimate the state of the quad-rotor; but it was computed off-board including SLAM algorithms. Therefore, it suffered with its wireless communication range.

In outdoor missions, LIDARs operate vertically to evaluate terrain levels[4] or horizontally to map obstacles.[9] In terrain mapping the amount of measurement data generally excludes onboard map processing or it requires a PC-based computer like in ref. [9]. Otherwise a cloud of points representing the terrain map is generated offline. This is commonly used to monitor trees growth in forests.[6,7] Terrain mapping can be also applied in SLAD—Safe Landing and Area Detection, even with real-time onboard processing (Yamaha R-Max).[3]

Additional interesting work[5] is about a 2D/3D outdoor obstacle avoidance method employing Kelly's grids, cubic Bezier curves, and a laser rangefinder with a pan/tilt module. To realize the method, authors used a powerful platform based on a Yamaha R-Max equipped with a dual flight computer, which has a high enough performance level to compute all necessary calculations and controls. Nevertheless, only simulation results are presented to prove the method its effectiveness. Another work[22] describes a successful application of a commercial 3D laser scanner installed into an identical helicopter which indicates that the Yamaha R-Max helicopter is favorite testing platform.

Therefore, a challengeable case of laser scanner application would be using it for outdoor missions on real fixed-wing mini UAVs. Seemingly it would require stabilizing the gimbals, which increases the payload, and further complicates the scanner framework, as in ref. [5]. Moreover, control algorithms for laser targeting are obligatory. There are some commercial 3D LIDARs (Fibertek Inc.) and flash LIDARs (SwissRanger SR 4000), but they are still too heavy for mini UAVs.[22]

To avoid these limitations, a concept of laser scanners for fixed-wing UAV is presented. It does not need gimbals to target laser beams, which results in a simplified framework, control algorithm, and data processing. This is a great advantage, which allows handling laser scanner operations easily and directly from a small autopilot system or advanced microcontroller. In addition, algorithms related with the processing of an occupancy map do not require complex and difficult computations to determine the reactive commands applied in obstacle avoidance. This proposed concept of a scanner should provide more accurate information about vehicle surroundings, and it will be able to track obstacles continuously and independently from actual vehicle attitude, unlike the case with two sensors.[20] Simultaneously, its compact framework makes it available for mini UAVs. Presented simulation results prove that the developed concept of the laser scanner may be a well-suited sensor for a wide variety of obstacle avoidance in outdoor scenarios, especially for flights through urban environments.

https://doi.org/10.1017/S0263574714001404 Published online by Cambridge University Press

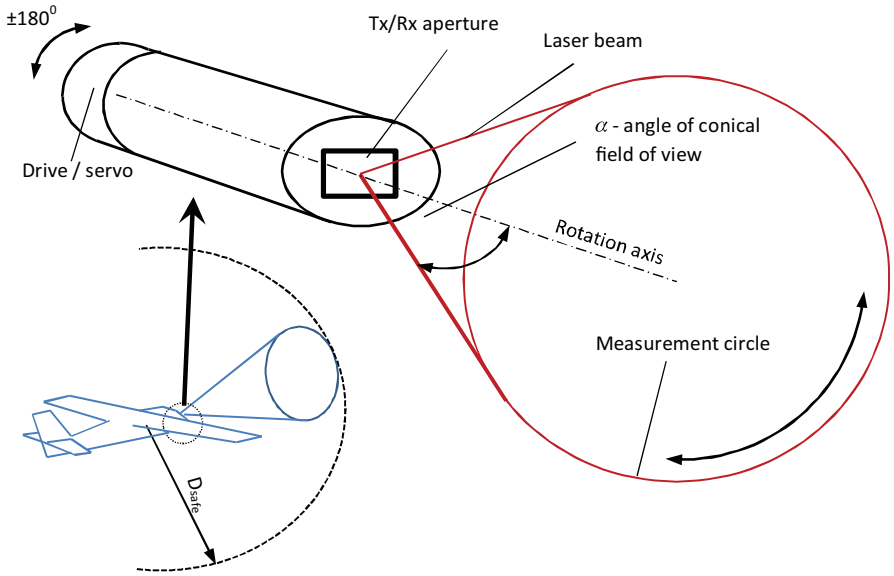

Fig. 1. The framework and the idea of the laser scanner concept: D_{safe}—a radius of the safety zone.

The article is split into six sections including the introduction. The first section, just after the introduction, presents a general idea of the laser scanner; especially it focuses on applicable hardware, proposed mechanical design, and on the principle of the scanner's operation. A selection of the cone angle and a problem of scanning cycle are also presented. In the next section there is a presentation of the algorithm of mapping and control that is essential to the use of the scanner in avoiding urban obstacles. Then, a structure of the simulation model and its related parameters are described. The results section presents two obstacle avoidance scenarios and delivers a discussion about results and effectiveness of the concept of the laser scanner. The article ends at the conclusions.

2. Laser Scanner Framework

The framework of the designed laser scanner is based on a miniature laser rangefinder (MLR100), whose transmitter aperture is fixed to the traversal profile of a cylinder. A detailed sensor description has been presented in pervious works.[12–14,20] Important parameters, which should be included here, are respectively, the measurement range over 150 m with a 20-cm accuracy, the repetition frequency of about 500 Hz, and output through UART. The sensor has two built-in filters: median and averaging, which eliminate faulty distance reports caused by incorrect laser beam reflections. The performance of the sensor has been already verified in reality. The cylinder is able to rotate in steps around the longitudinal axis in a range of 360°. An angle between the traversal profile and the rotation axis defines the scanner's conical field of view (Fig. 1). The rotation axis has to be parallel to the longitudinal axis of the UAV's body.

The angle of conical field of view is defined directly by two parameters: a ground projection of a minimum turn radius R_{T}—specific for each vehicle posture and maneuvering possibilities; and W_{O}—a minimum width of expected obstacles. It can be derived from the following relation:$\alpha = \frac{1}{2} \times \arccos(\frac{2R_{\text{T}}-W}{2R_{\text{T}}})$, whose geometrical explanation can be found in Fig. 2. Because the cone angle is related with a known dynamics of the vehicle and with a typical width of urban obstacles, it could be fixed permanently to reduce a total weight of the scanner and to simplify a mechanical design.

The cylinder can be driven by a digital servo with an operating range of 360°. Digital servos are the best way to control rotation steps precisely. Splitting rotation into a limited number of steps reduces the amount of measurement points, which are next processed by an onboard processor without the computational overload. Undoubtedly, a high number of measurement points increases the scanner resolution; but on the other hand it also increases the duration of the 360°-range scanning cycle. The operations of the miniature laser rangefinder are controlled through a serial port. Hence, transmitting a measurement command as two bytes, receiving a distance value as four bytes, and the

https://doi.org/10.1017/S0263574714001404 Published online by Cambridge University Press

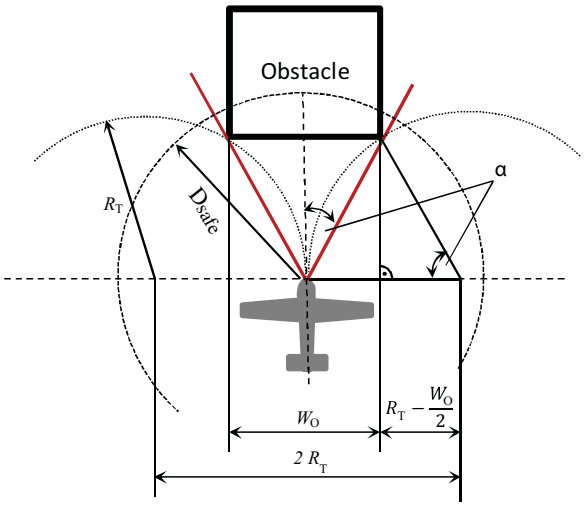

Fig. 2. The idea of selection of the cone angle: R_T—a ground projection of a minimum turn radius related with the vehicle's dynamics; W_O—a typical minimum width of urban obstacle; D_{safe}—the radius of the safety zone.

most important—the time for a single rotation step, altogether multiplied by the resolution, can result in a relatively long processing time. Hence, a compromise between the resolution and the scanning cycle period should be made. In the paper we assumed that 16 points give enough information about the occupation of the vehicle's frontal area to enable the possibility of safe avoidance. Also, we forecast that the period of a single scanning cycle should be approximately 1 s, if we assume that a typical digital servo's speed is 0.13 s/60°, a baud rate of 57600 bps guarantees 0.13 ms for one-byte transmission, and the minimum time required for a single distance measurement is 2 ms (1/500 Hz). It is a fair value, if we take under consideration that the typical maximum speed of mini-UAV-level flight is about 50 km/h. The relation between the resolution and scanning cycle interval is given by

$$T = R \times \left(t_{\mathrm{m}} + L \times t_{\mathrm{t}} + \frac{360^{\circ}}{V \times R} + T_{\mathrm{C}} \right), \tag{1}$$

where:

T = interval of a single 360° scan,

R = resolution of the laser scanner,

t_m = duration of a single measurement (min. 2 ms),

t_t = duration of one-byte transmission over universal asynchronous receiver/transmitter (UART; 0,138 ms at 57600 bps),

L = total number of bytes transmitted from/to the laser rangefinder (four for result + two for command),

V = servo rotation speed (approximately 461°/s),

T_C =computation time, including the update of output commands (much less than 1 ms if CPU is running at e.g. 168 MHz).

The computation time is relatively small if compared to the overall duration of a scanning cycle. Most of the required calculations are composed with arithmetic operations like addition and multiplication applied on small matrices of integers. The size of these matrices is related to the resolution and is much lower versus sizes of video frames. The construction of the occupancy grid is also simple, since the cells contain differences between the measured distance and D_{safe}—the given radius of the safety zone. Moreover, if we assume that modern microcontrollers are supported by floating processing units (FPU), interrupt services, and a direct memory access (DMA) technique, calculations have no impact on scanning performance. It is rather related with the maximum servo speed and this simply limits the real-time operation of the scanner. Another issue is a blind spot inside

https://doi.org/10.1017/S0263574714001404 Published online by Cambridge University Press

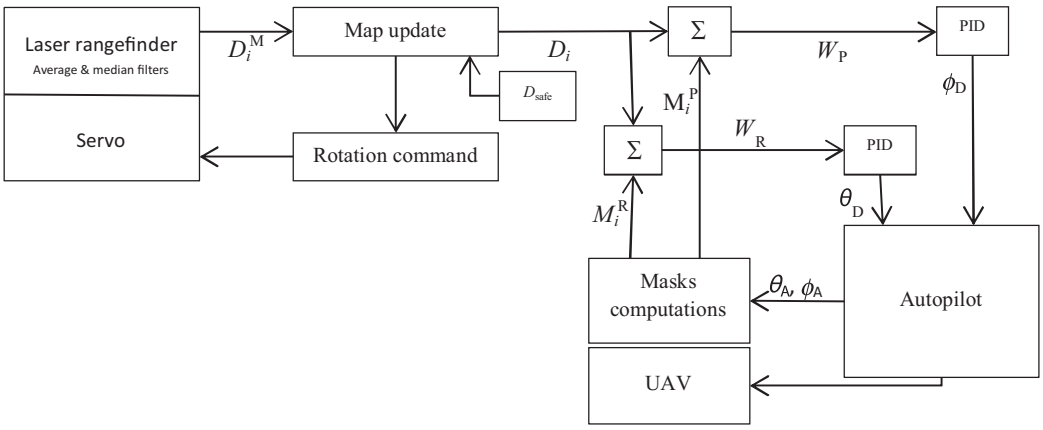

Fig. 3. A structure of the mapping and control algorithm applied in the concept of the laser scanner: D_i^M—a single distance measurement related with the ith cell of the map, D_i—a content of the ith cell of the occupancy map, D_{safe}—the radius of the safety zone, M_i^R—the ith element of the mask for a roll control, M_i^P—the ith element of the mask for a pitch control, W_R, W_P—sums of the products of elements of the map and associated mask, θ_D—desired pitch angle, ϕ_D—desired roll angle, θ_A—actual pitch angle, ϕ_A—actual roll angle.

the cone, making UAV blind to small flying objects. Therefore, the main purpose of the scanner is to detect immovable ground-rooted obstacles, which are typical for uncertain urban environments.

The major factor that decides about accuracy of the scanner and eventual errors is a mechanical design and the precision of servo positioning. The laser rangefinder offers enough accurate and reliable distance measurement to minimize final error of the scanner. Only experiment allows discussing this issue thoroughly.

3. Mapping and Control Algorithm

The diagram of the overall mapping and control algorithm is presented in Fig. 3. Each element of the algorithm will be successively discussed in detail later in this section.

The full scanning cycle containing R measurement points will result in an occupancy map which could be represented as a circular grid of R cells (similar to an occupation grid). It is co-centered and normal to the longitudinal axis of the UAV's body, and lies on a plane projected in the vehicle front. Such formulation of the map is not only coherent with the measurement geometry, but also gives information about the obstacle's location in relation to actual velocity vector. Synergizing an obstacle's relative location with the measured distances provides enough information to control the vehicle in 3D obstacle avoidance. The diagram of the map acquired in a single scanning cycle for $R = 16$ is presented in Fig. 4.

Cells of the map from Fig. 4 have the distance from an obstacle location to the border of the safety zone defined by a sphere around UAV indicated by D_{safe} radius (Fig. 1). So, if the obstacle is outside the sphere, the D_i cell of the map will be equal to zero. Otherwise, D_i identifies how far the obstacle is positioned from the border of the safety zone, and it reaches the highest value for the closest obstacle. The value of D_i is described as follows:

$$D_i = \begin{cases} D_{safe} - D_i^M & D_i^M \leq D_{safe} \\ 0 & D_i^M > D_{safe} \end{cases}, \tag{2}$$

where: D_i^M = distance measured by the laser scanner (max 150 m for MLR100), D_{safe} = radius of the spherical safety zone around the UAV ($D_{safe} \leq \max D_i^M$).

The sphere radius is given by

$$D_{safe} = \frac{H_{max}^{OB}}{\tan(\theta_{max}) \times \cos(\alpha)}, \tag{3}$$

https://doi.org/10.1017/S0263574714001404 Published online by Cambridge University Press

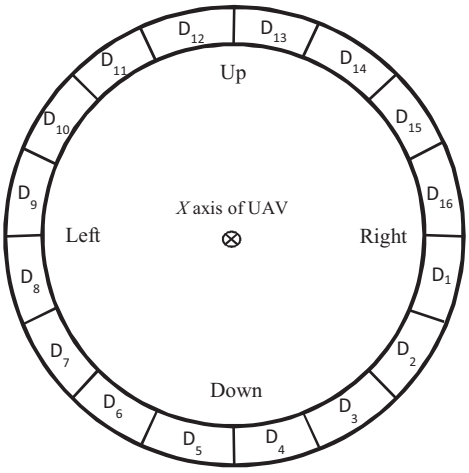

Fig. 4. The graphical representation of the map (occupation grid) acquired in a single scanning cycle.

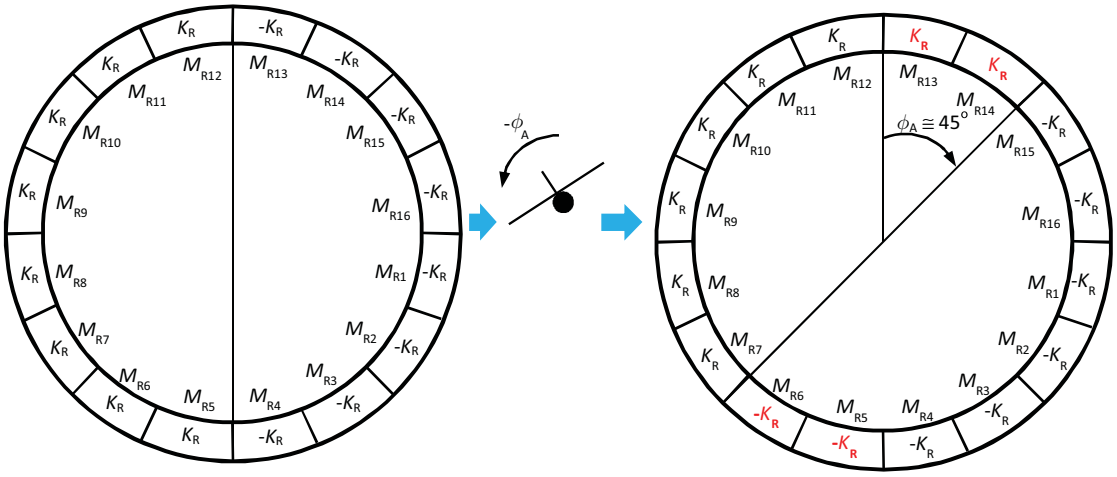

Fig. 5. The illustration of the mask structure for the roll control and the rotation rule: M_{Ri} =the ith cell of the mask; $\pm K_R$ =gain value. According to Eq. (4), for $\phi_A \cong 45^\circ N = 2$, $M_{R7} \div M_{R14} = K_R$, $M_{R1} \div M_{R6} = -K_R$, and $M_{R15} \div M_{R16} = -K_R$.

where:

$H_{\max OB}$ = maximum obstacle height,
$\theta_{\max}$ = maximum UAV pitch angle (max $\pm 30^\circ$),
α = angle of the scanner's conical field of view.

Consequently, the map is ready to be utilized in a control algorithm. To generate the required commands for pitch and roll controls, it is necessary to apply two special masks to the map. These masks compensate the vehicle attitude and calculate the two independent parameters that are directly related to roll and pitch commands. The first mask is for a roll angle control, and the second is for a pitch angle control. The mask structure for the roll control is presented in Fig. 5. Cells of the mask have a meaning of a signed gain. The mask is rotating contrariwise to the UAV's rotation. Hence, the impact of UAV's roll angle on the map rotation is able to be compensated (Eq. (4)). The formula for the mask rotation is as follows:

$$M_i^{\mathrm{R}}(\phi_{\mathrm{A}}) = \begin{cases} K_{\mathrm{R}} \to i \in \frac{R}{4} + N + 1, \quad \frac{3\times R}{4} + N, \quad N = \mathrm{round}\left(\frac{\phi_{\mathrm{A}} \times R}{360^\circ}\right) \\ -K_{\mathrm{R}} \to i \in 1, \quad \frac{R}{4} + N \cap^i \in \frac{3\times R}{4} + N + 1, \quad R, N = \mathrm{round}\left(\frac{\phi_{\mathrm{A}} \times R}{360^\circ}\right) \end{cases}, \tag{4}$$

https://doi.org/10.1017/S0263574714001404 Published online by Cambridge University Press

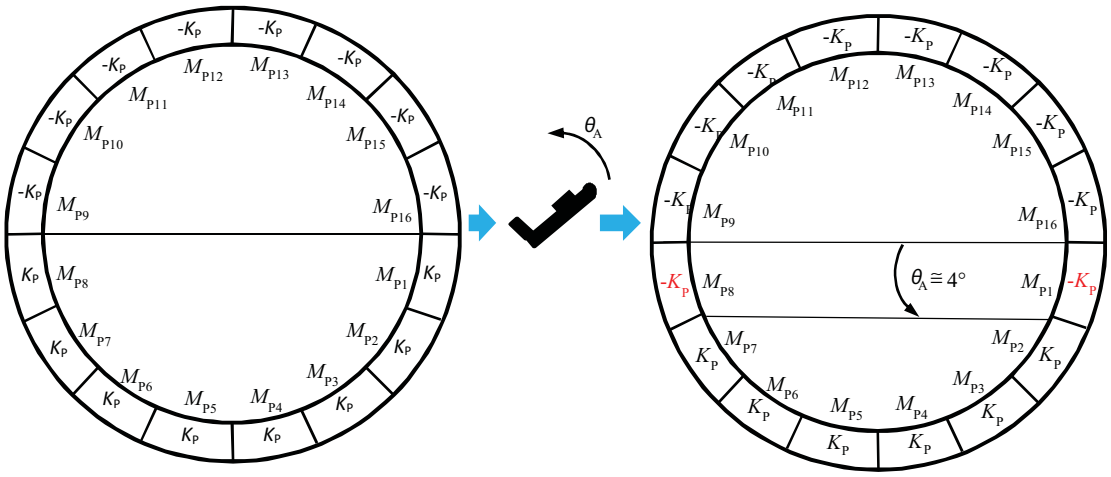

Fig. 6. The illustration of the mask structure for pitch control and the shifting rule: M_{Pi} = the ith cell of the mask, $\pm K_P$ = gain value. According to Eq. (5), for $\theta_A \cong -4^\circ S = 1$, $M_{P2} \div M_{P7} = K_P$, $M_{P8} \div M_{P16} = -K_P$ and $M_{R16} = -K_P$.

where:

R = resolution of the laser scanner, i.e. the number of measurements per 360° range of the scanning cycle (power of 2),

K_R = gain value used in the mask for roll control,

$M_i^R(\phi_A)$ = gain value in the ith cell of the mask after the rotation,

N = number of cells equivalent to the actual roll angle,

ϕ_A = actual UAV roll angle.

Thus, the sign change line that splits the mask into two regions, remains perpendicular to the horizon line at any roll angle. In the case of the mask for pitch control, this line must be parallel to the horizon line. Only then the impact of the actual pitch angle on the map shift is compensated. Hence, the sign change line is shifted proportionally to the actual pitch in reverse vertical direction. The structure of the mask for pitch control and the idea of shifting are presented in Fig. 6.

The formula for the map shifting is as follows:

$$M_i^P(\theta_A) = \begin{cases} K_P \rightarrow \left(i \in 1+S, \quad \frac{R}{2} - S, S \geq 0\right) \cup \left(i \in 1, \quad \frac{R}{2} - S \cap R + S + 1, \quad R, S < 0\right), \\ -K_P \rightarrow \left(i \in \frac{R}{2} - S + 1, \quad R \cap 1, \quad S, S > 0\right) \cup \left(i \in \frac{R}{2} - S + 1, \quad R + S, S \leq 0\right), \\ S = \text{round}\left(\frac{\theta_A \times R}{4 \times \alpha}\right), \end{cases} \tag{5}$$

where:

R = resolution of the laser scanner, i.e. the number of measurements per 360° range of the scanning cycle (power of 2),

K_P = gain value used in the mask for pitch control,

$M_i^P(\theta_A)$ = gain value in the ith cell of the mask after the shifting,

S = number of cells equivalent to the actual pitch angle,

α = angle of the scanner's conical field of view,

θ_A = actual pitch angle.

When both masks have been modified according to actual roll and pitch angles, they are ready to be applied to the map, i.e. the sum of multiplications, between the ith cell of the map and corresponding the ith cell of the mask, is calculated. Everything is processed separately for each mask. Finally, it will result in two parameters that are directly related to pitch and roll commands required for obstacle

https://doi.org/10.1017/S0263574714001404 Published online by Cambridge University Press

avoidance. These parameters are defined by the following expressions:

$$W_{\mathrm{R}} = \sum_{i=1}^{R} D_i \times M_i^{\mathrm{R}}(\phi_{\mathrm{A}}), \tag{6}$$

$$W_{\mathrm{P}} = \sum_{i=1}^{R} D_i \times M_i^{\mathrm{P}}(\theta_{\mathrm{A}}), \tag{7}$$

where:

W_{R} = desired roll bounded to the vehicle's stability range, e.g. $\pm 30^{\circ}$,
W_{P} = desired pitch bounded to the vehicle's stability range, e.g. $\pm 30^{\circ}$,
R = resolution of the laser scanner, i.e. the number of measurements per 360° range of the scanning cycle (power of 2),
D_i = content of the ith cell in the occupation grid (map),
$M_i^{\mathrm{P}}(\theta_{\mathrm{A}})$ = gain value in the ith cell of the mask after shifting,
$M_i^{\mathrm{R}}(\phi_{\mathrm{A}})$ = gain value in the ith cell of the mask after rotation.

Next, W_{R} and W_{P} can be considered as error signals for the two separate proportional-integral-derivative (PID) loops, which finally generate signals of the desired roll and desired pitch. The signals are routed directly to a low-level control of the flight computer to realize an avoidance maneuver. PID loops are sufficient to minimize the values of W_{R} and W_{P}, which equal to zero, if there are no obstacles around the flight path, i.e. all cells of the map are also zero.

4. Simulation

To assess the usability of the proposed concept of the laser scanner, a simulation model was prepared in a MATLAB / SIMULINK environment. In the model, we considered a simple UAV's kinematics sufficient enough for the purpose of research. This is due to the fact that the obstacle avoidance control based on the laser scanner will operate over the low-level control of the flight computer. So it does not relate to the vehicle's dynamics directly. Besides, the low-level control has to be set up separately for each type of vehicle. Therefore, in simulations we reduce the problem of the UAV's dynamics to the first order of inertia as a result of the low-level control supported by the autopilot. Hereby, we are able to put more attention on kinematics defined by the following parameters: relative coordinates, orientation angles, and flight speed. The model inputs switch between the outputs of the two control subsystems: obstacle avoidance subsystem and waypoint navigation subsystem. It is dependent on the actual state of the occupancy map. The differential equations of the applied UAV's kinematics are as follows:[13]

$$\begin{aligned}
\dot{x} &= V \times \cos\psi \times \cos\theta, \\
\dot{y} &= V \times \sin\psi \times \cos\theta, \\
\dot{z} &= V \times \sin\theta, \\
\dot{\psi} &= \frac{g}{V} \times \tan\varphi, \\
\dot{\varphi} &= \alpha_{\varphi}(\varphi^{\mathrm{C}} - \varphi), \\
\dot{\theta} &= \alpha_{\theta}(\theta^{\mathrm{C}} - \theta), \\
\dot{V} &= \alpha_{V}(V^{\mathrm{C}} - V).
\end{aligned} \tag{8}$$

where:

x, y, z = the UAV's relative coordinates,
ψ, ϕ, θ = the UAV's actual attitude: heading, roll, and pitch,
$\psi^{\mathrm{C}}, \phi^{\mathrm{C}}, \theta^{\mathrm{C}}$ = attitude commands: desired heading, desired roll, and desired pitch,
$\alpha_{\psi}, \alpha_{\phi}, \alpha_{\theta}$ = dynamic time constants,

https://doi.org/10.1017/S0263574714001404 Published online by Cambridge University Press

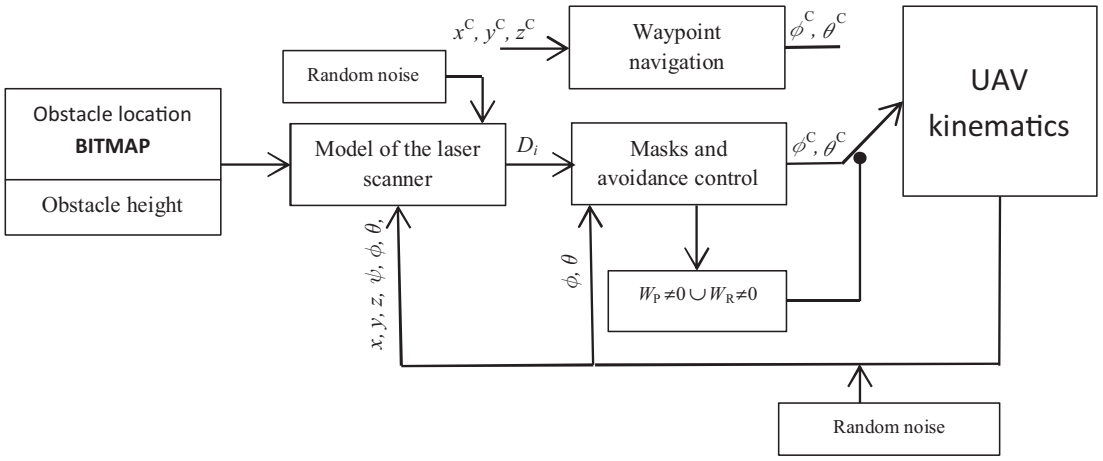

Fig. 7. The structure of the simulation model.

g = gravitational acceleration,
V = actual flight speed,
V^C = speed command (approx. 12 m/s).

To control the UAV's velocity vector in the simulations, we prepared a simple model for the waypoint navigation subsystem. This model exploits the output of a PID controller as a source of the desired heading, while the heading error, i.e. the bearing between the current UAV's location and the target waypoint, is the model's input. The model for the waypoint navigation control is given by[13]

$$\begin{aligned}
\psi^C &= \arctan\left(\frac{y^C - y}{x^C - x}\right) \\
\psi^E &= \psi^C - \psi, \\
\varphi^C &= PID(\psi^E) \\
\theta^C &= \arctan\left(\frac{z^C - z}{\sqrt{(y^C - y)^2 + (x^C - x)^2}}\right),
\end{aligned} \tag{9}$$

where:
x^C, y^C, z^C = the target waypoint's coordinates,
x, y, z = the current UAV's coordinates,
ψ^E = heading error (bearing),
ϕ^C = roll command (max $\pm 30^\circ$),
θ^C = pitch command (max $\pm 30^\circ$).

Naturally, we also modeled the operation of the laser scanner including an associated obstacle avoidance control. To add uncertainty to the system we apply random noises, which are included in measurement signals of distance, the UAV's attitude and position. Noises and measurement errors mostly come from external disturbances like a wind or limited accuracy of onboard sensors. According to a specification of the laser rangefinder and our experience from its real usage in flight, we can assume that the magnitude of random error for this sensor should be below ± 0.5 m. In the case of UAV's attitude and position, this value should be respectively below $\pm 4.5^\circ$ and ± 2 m (in real flight). A cumulative random error of distance measurement reported during real flight can reach even ± 5 m.

To simulate the obstacle mapping, it was necessary to prepare the flight environment with a 3D obstacle. It was possible owing to the bitmap representation of the obstacle's horizontal projection and information about the obstacle's height. The structure of the entire simulation model is shown in Fig. 7.

https://doi.org/10.1017/S0263574714001404 Published online by Cambridge University Press

The proposed simulations are expected to identify limitations of the concept; especially they should answer if the concept is resistive to volatile relative positions and orientations between a vehicle and an obstacle, while the scanning interval is equal to 1 s. Additionally, the results should deliver information, which will be helpful in an analysis of the applicability of the concept in the flights through urban environments.

5. Results

The flight environments applied in the simulations were composed with a single cuboidal obstacle located near the center of the scene. Such a ground-rooted obstacle is typical in urban environments. Its vertical and horizontal edges are well suited for tests of the effectiveness of obstacle avoidance in a wide variety of possible collision scenarios considering different relative positions and orientations. To verify the concept thoroughly, we created two sets of pairs of points defining the collision courses' lines. These lines intersect with an obstacle wall at different places and at different angles. A single pair of points is defined by a starting point and a target waypoint. Each set of the pairs of points is used to compose two different simulation scenarios, which differs in flight courses. Both of them have the same objective, which is to observe how UAV realizes flight between two specified waypoints. The set of the pairs of points for the first scenario is given by

$$A = \left\{(x_1, y_1 + i \times y), (x_2, y_2 + i \times y) : x_1 = 100,\ x_2 = 900,\ y_{1,2} = 260, = 20,\ i = 1, \ldots, 6\right\}. \tag{10}$$

In the simulation we also assumed the following: the angle of the scanner's field of view is equal to 15°, the maximum obstacle height is equal to 30 m, the initial heading is equal to 0°, and the flight speed is about 10 m/s. Gain values in both the masks, i.e. K_P and K_R, were set to be equal to 2. The ranges of roll and pitch angles were limited to ±30°, which is typically bound for stable flight of mini UAVs controlled by an autopilot. A delay between two successive distance measurements was included in the laser scanner model, and it was set to 1/16 of a second to achieve one full scanning cycle per second. Figure 8 presents the flight paths collected during the simulation.

Figure 9 presents plots of the selected control signals for the course defined by relation $y_0 = y_{wp} = 280$. These signals are the desired roll, the desired pitch, and the sums of the map cells lying on both sides of the sign change lines in each mask. The plots of the signals are a clear proof of reliable operations of the obstacle avoidance control based on the concept of the laser scanner. The UAV is able to achieve a 3D avoidance realized by simultaneous control for roll and pitch, i.e. turning and climbing.

The second set of pairs of points used to simulate the collision paths is defined by expression (11). This time the angle between the course line and the obstacle's wall plane is different from 90°, what enables the case, when a UAV flies directly towards the vertical edge of an obstacle. It is the hardest case for the concept, because the edge may appear too close to the vehicle as a result of the conical field of view. A further consequence of the case is a loss of reserve of distance needful to achieve safe avoidance.

$$\begin{aligned} B = \{&(x_1 + i\times, y_1), \quad (x_2 + i \times y, y_2) : x_1 = 140, \quad x_2 = 740, \\ &y_1 = 100, y_2 = 600, = 20,\ i = 1, \ldots, 13\}. \end{aligned} \tag{11}$$

Figure 10 presents another set of trajectories, which deals with the criteria of safe obstacle avoidance. Also, this time the vehicle keeps a safe distance from the obstacle, according to the responses of both the pitch and roll controls. It is possible to track that the vehicle started to turn and climb simultaneously. Especially, it is clearly seen on the plots of roll and pitch from Fig. 11. Therefore, the designed laser scanner is an effective information source for the 3D flight controls.

Next figure (Fig. 12) presents a more complicated scenario composed with a group of five obstacles located one by one. Also, this time the proposed concept does not fail.

Summarizing, the received results of the simulations show that the vehicle is able to avoid obstacles safely and independently from the actual relative obstacle's positions and the vehicle attitude. It is a beneficial feature; because other approaches based on a spot measurement often fail in some cases.

https://doi.org/10.1017/S0263574714001404 Published online by Cambridge University Press

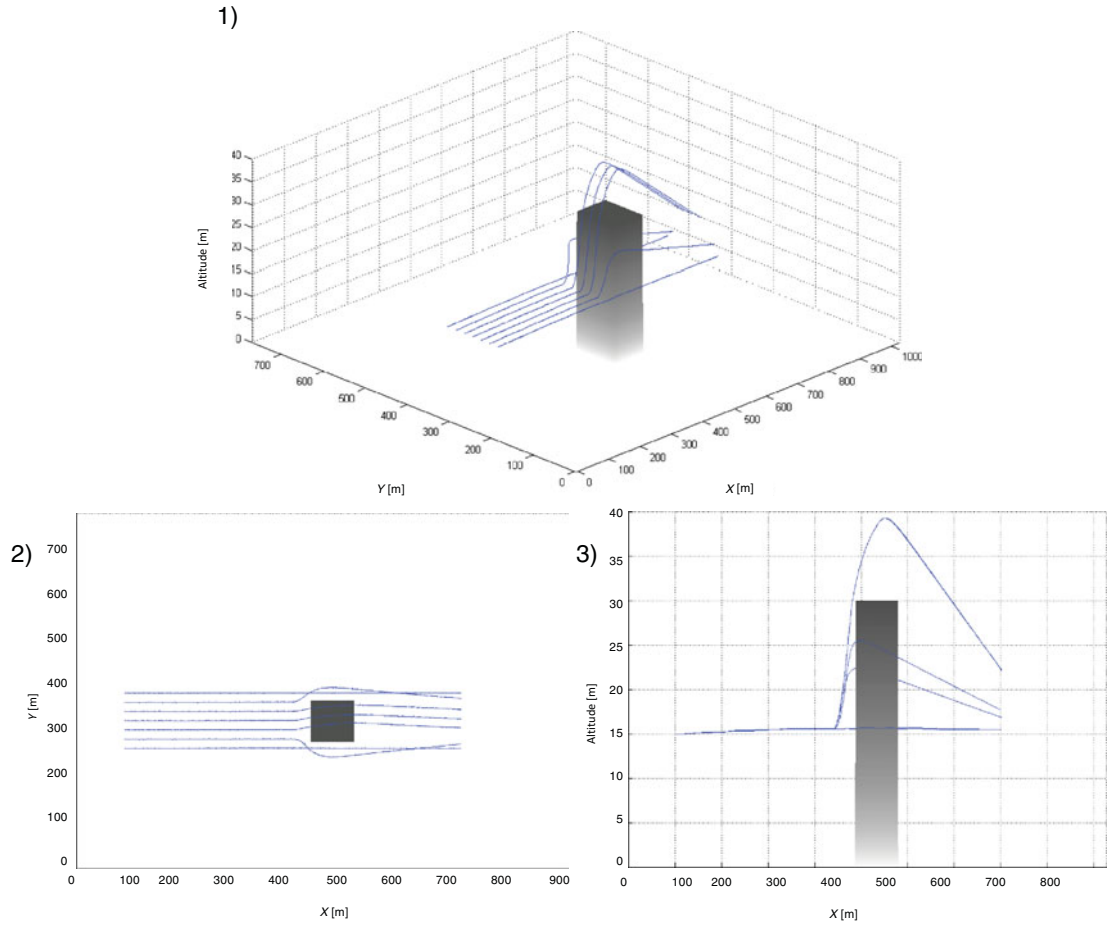

Fig. 8. The flight paths present the simulation of 3D avoidance maneuvers for set *A*: (1) the 3D flight paths; (2) the horizontal view; (3) the vertical view.

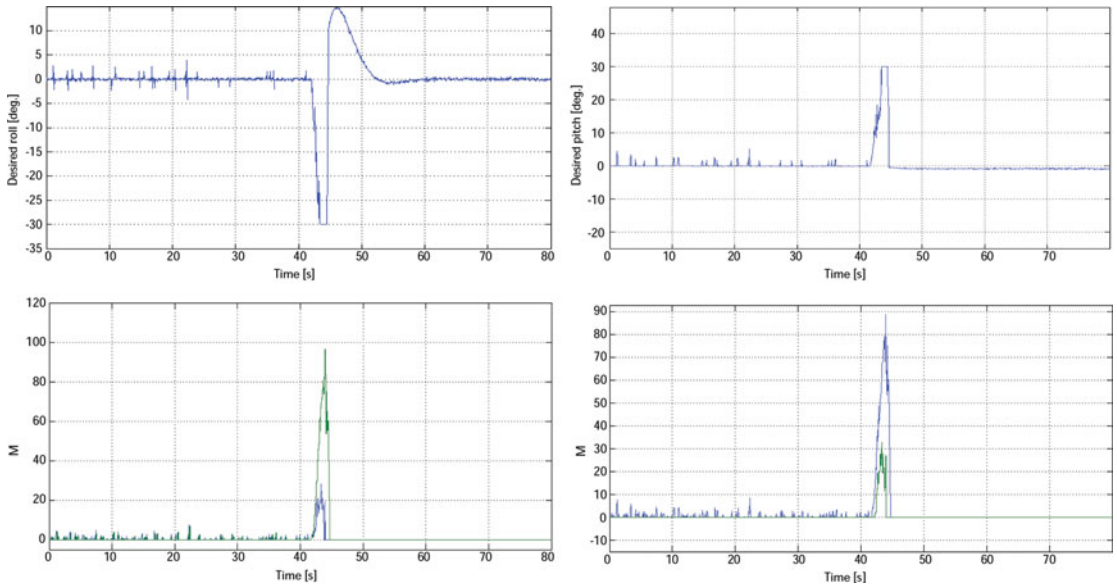

Fig. 9. Plots of the control signals for the course defined by $y_0 = y_{wp} = 280$: (1) desired roll; (2) desired pitch; (3) $\sum_{i=1}^{4} D_i + \sum_{i=13}^{16} D_i$ (blue) and $\sum_{i=5}^{12} D_i$ (green); (4) $\sum_{i=1}^{8} D_i$ (blue) and $\sum_{i=9}^{16} D_i$ (green).

https://doi.org/10.1017/S0263574714001404 Published online by Cambridge University Press

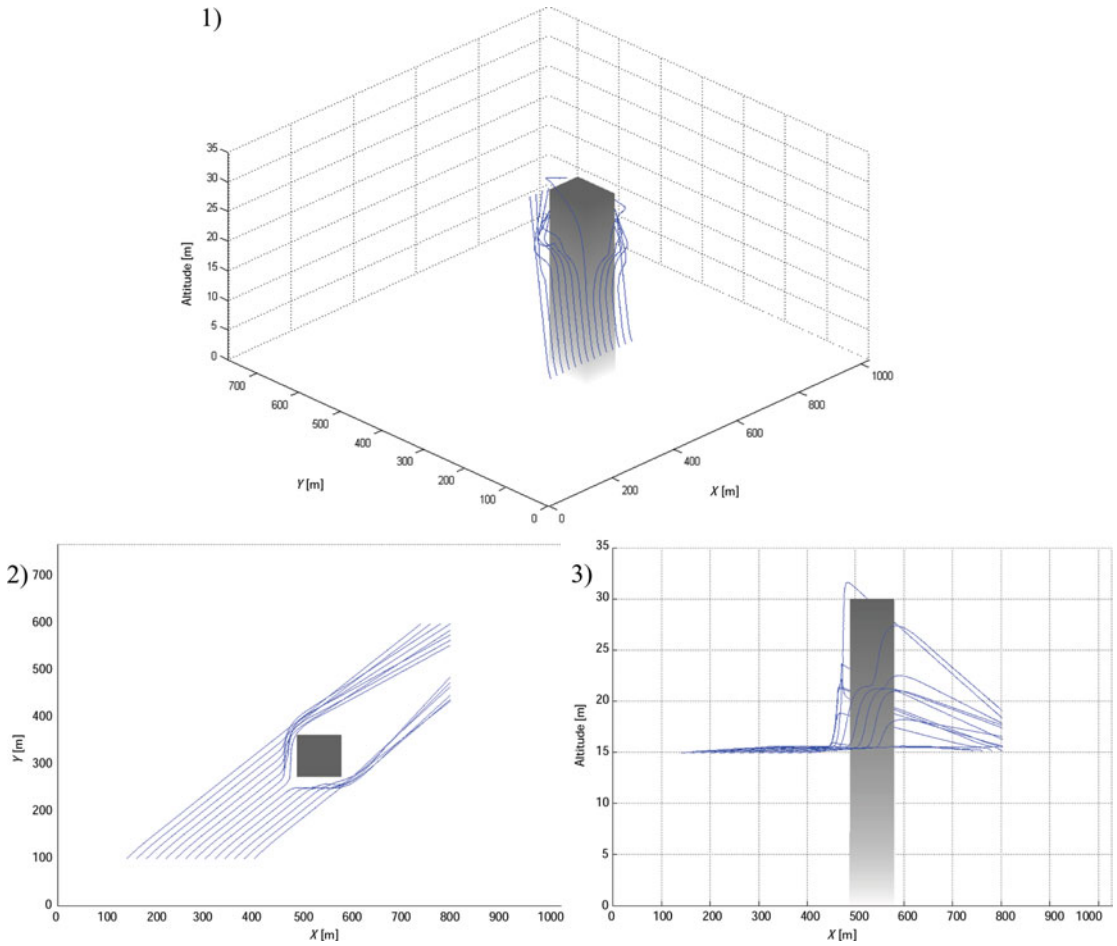

Fig. 10. The flight paths present simulation of 3D avoidance maneuvers for set *B*: (1) the 3D flight paths; (2) the horizontal view; (3) the vertical view.

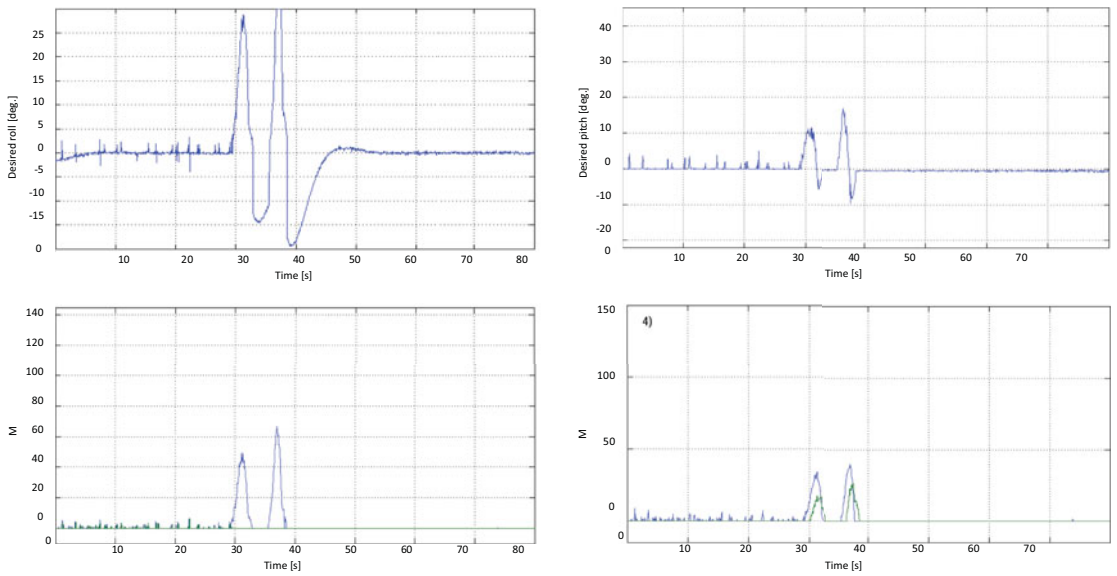

Fig. 11. Plots of the control signals for the course defined by $x_0 = 260$, $y_0 = 100$, $x_{wp} = 860$, $y_{wp} = 600$: (1) desired roll; (2) pitch; (3) $\sum_{i=1}^{4} D_i + \sum_{i=13}^{16} D_i$ (blue) and $\sum_{i=5}^{12} D_i$ (green); (4) $\sum_{i=1}^{8} D_i$ (blue) and $\sum_{i=9}^{16} D_i$ (green).

https://doi.org/10.1017/S0263574714001404 Published online by Cambridge University Press

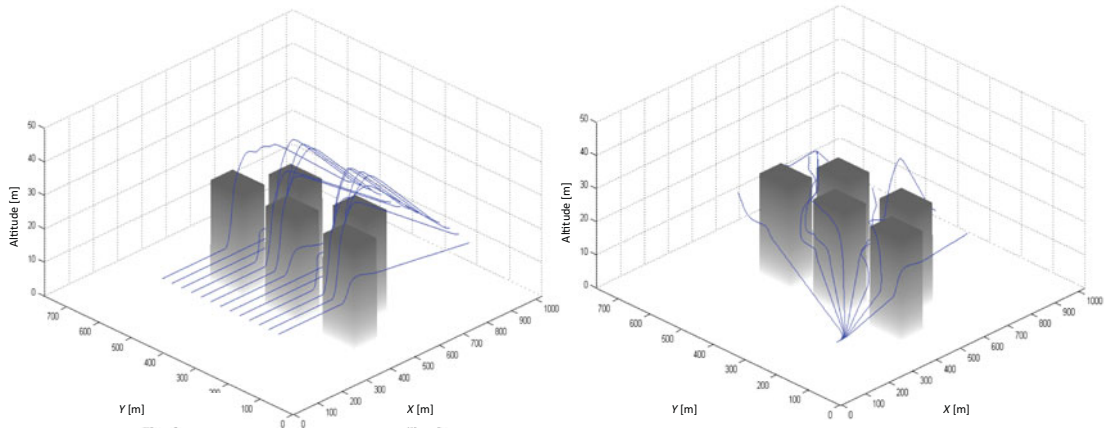

Fig. 12. Flights through the group of five obstacles.

After carefully analyzing all the flight paths presented in Figs. 7 and 9, we concluded that some of them could be too close to the obstacle. This is an effect of bounded angles of pitch and roll, which guarantee the vehicle's stability and it is true only if the low-level control is accurately adjusted to prevent these bounds overshot.

To achieve a safer distance between the vehicle and the obstacle, the avoidance maneuver should start earlier. Hence, the radius of the safety zone used to calculate the occupancy grid, or gain values in the masks should be increased to receive a faster prediction of an avoidance maneuver. The limited range of pitch and roll angles effect on the safety of obstacle avoidance are stronger than the inertia in the vehicle's dynamics, what is confirmed by high dynamics maneuvers of the vehicle. At this moment, it should be highlighted, that observed turn radius of about 40 m and altitude change of 15 m at a distance of about 40 m are a typical performance of small vehicles.[14] Applying wider ranges of allowable roll and pitch angles combined with the vehicle's dynamics increases the risk of total instability of the system. Therefore, to achieve the best performance of the proposed scanner, the UAV's low-level control should be preliminarily adjusted to provide a safe reserve of stability for the widest possible range of pitch and roll angles.

6. Conclusion

It is very difficult to create a simple and reliable obstacle detection system for fixed-wing UAVs. Most of the laser scanner applications in the field of UAVs focus on holonomic flying robots, which simplifies the terrain mapping by avoiding real-timeframe translations applied to a high number of coordinates. Moreover, in some cases gimbals partially solve the problem of sensor stabilization; so the sensor targeting algorithm is still expected.

The article presents an innovative concept of the laser scanner designed for a fixed-wing UAV. It does not require any frame translation or gimbals. Furthermore, a limited amount of data will not overload the onboard flight computer. On the other hand the laser scanner will provide enough information about the occupancy of the UAV's surroundings to enable the 3D guidance. The simulation results are an obvious evidence for the effectiveness of obstacle avoidance. The vehicle is able to change its heading and altitude as a result of the pitch and roll controls based on the map processing, yet a delay between two successive measurements does not disturb the flight guidance to achieve a completely safe avoidance. The effectiveness of the avoidance maneuver is dependent on such parameters as the allowable range of roll (minimum turn radius) and pitch angles (climbing rate), or the maximum radius of the safety zone—D_{safe} (avoidance prediction).

Summarizing, the concept seems to be very promising, and it certainly will be realized on the basis of a miniature laser rangefinder MLR100 as shown in Fig. 13. Only an experiment with the scanner prototype will validate reliably its real performance.

https://doi.org/10.1017/S0263574714001404 Published online by Cambridge University Press

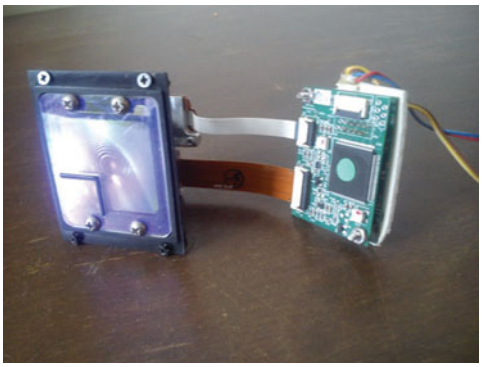

Fig. 13. The miniature laser rangefinder—MLR100 from Flir System (Aerius).

References

1. S. Grzonka, G. Grisetti and W. Burgard, "Towards a Navigation System for Autonomous Indoor Flying," *Proceedings of the IEEE International Conference on Robotics and Automation*, Kobc, Japan (May 12–17, 2009) pp. 2878–2883.
2. M. Sanfourche, G. L. Besnerais, P. Fabiani, A. Piquereau and M. S. Whalley, "Comparison of Terrain Characterization Methods for Autonomous UAVs," *Proceedings of the 65th Annual Forum of the American Helicopter Society*, Grapevine, Texas, USA (May 27–29, 2009) pp. 1–14.
3. M. Whalley, M. Takahashi, P. Tsenkov and G. Schulein, "Field-Testing of a Helicopter UAV Obstacle Field Navigation and Landing System," *Proceedings of the 65th Annual Forum of the American Helicopter Society*, see ref. 2.
4. Y. Lin, J. Hyyppa and A. Jaakola, "Mini-UAV-Borne LIDAR for fine-scale mapping," *IEEE GeoSci. Remote Sens. Lett.* **8**(3), 426–430 (2011).
5. M. S. Geyer and E. N. Johnson, "3D Obstacle Avoidance in Adversarial Environments for Unmanned Aerial Vehicles," *Proceedings of AIAA Guidance, Navigation, and Control Conference and Exhibit*, Keystone, USA (Aug. 21–24, 2006) (chapter AIAA 2006-6542).
6. L. O. Wallace, A. Lucieer and C. S. Watson, "Assessing the feasibility of UAV-based LIDAR for high resolution, forest change detection, international archives of the photogrammetry," *Remote Sens. Spat. Inf. Sci.* **XXXIX-B7**, 499–504 (2012).
7. L. O. Wallace, A. Lucieer, C. S. Watson and D. Turner, "Development of a UAV-LiDAR system with application to forest inventory," *Remote Sens.* **4**, 1519–1543 (2012).
8. S. E. Hrabar, "3D Path Planning and Stereo-based Obstacle Avoidance for Rotorcraft UAVs," *Proceedings of the IEEE/RSJ International Conference on Intelligent Robots and Systems*, Nice, France (Sep. 22–26, 2008) pp. 807–814.
9. S. Harbar, "Reactive Obstacle Avoidance for Rotorcraft UAVs," *Proceedings of the IEEE/RSJ International Conference on Intelligent Robots and Systems*, San Francisco, USA (Sep. 25–30, 2011) pp. 4967–4974.
10. S. E. Hrabar and G. S. Sukhatme, "Vision-based navigation through urban canyons," *J. Field Robot.* **26**(5), 431–452 (2009).
11. A. Beyeler, J. C. Zufferey, D. Floreano, "Vision based control of near-obstacle flight," *Auton. Robots* **27**(3), 201–219 (2009).
12. C. Kownacki, "Guidance and Obstacle Avoidance of MAV in Uncertain Urban Environment," *Proceedings of the 2009 European Micro Aerial Vehicle Conference and Flight Competition,* Delft, the Netherlands (Sep. 14–17, 2009), online only.
13. C. Kownacki, "Obstacle Avoidance Strategy for Micro Aerial Vehicle," **In**: *Advances in Aerospace Guidance, Navigation and Control* (F. Holzapfel and S. Theil, eds.) (Springer-Verlag, Berlin, 2011) pp. 117–135.
14. C. Kownacki, "Successful application of miniature laser rangefinders in obstacle avoidance method for fixed wing UAV," *Int. J. Robot. Autom.* **28**(3), 292–298 (2013).
15. S. Todorovic and M. C. Nechyba, "A vision system for intelligent mission profiles of micro air vehicles," *IEEE Trans. Veh. Technol.* **53**(6), 1713–1725 (2004).
16. S. Griffiths, J. Saunders, A. Curtis, B. Barber, T. McLain and R. Beard, "Obstacle and Terrain Avoidance for Miniature Aerial Vehicles," **In**: *Advances in Unmanned Aerial Vehicles, State of the Art and the Road to Autonomy* (K. P. Valavanis, ed.) (Spinger, 2007) pp. 213–244.
17. P. Campoy, J. F. Correa, I. Mondragón,C. Martínez, M. Olivares, L. Mejías, J. Artieda, K. Valavanis, P. Oh and L. Piegl, "Computer Vision Onboard UAVs for Civilian Tasks," **In**: *Unmanned Aircraft Systems* (K. P. Valavanis, P. Oh, L. A. Piegl, eds.) (Springer, Netherlands 2009) pp. 105–135.
18. F. Andert, F. Adolf, L. Goormann and J. Dittrich, "Autonomous vision-based helicopter flights through obstacle gates," *J. Intell. Robot. Syst.* 259–280 (2010).
19. Y. Watanabe, A. Calise and E. N. Johnson, "Vision-Based Obstacle Avoidance for UAVs," *Proceedings of AIAA Guidance, Navigation and Control Conference and Exhibit*, Hilton Head, USA (Aug. 20–23, 2007) (Chapter AIAA 2007-6829).

https://doi.org/10.1017/S0263574714001404 Published online by Cambridge University Press

20. C. Kowacki, "Successful application of miniature laser rangefinders in obstacle avoidance method for fixed wing micro UAV," *Int. J. Robot. Autom.*, **28**(3), 292–298 (2013).
21. M. Achtelik, A. Bachrach, R. Heb, S. Prentice and N. Roy, "Stereo Vision and Laser Odometry for Autonomous Helicopters in GPS-denied Indoor Environments," *Proceedings of the 11th SPIE Unmanned Systems Technology*, vol. 7332 733219, Orlando, Florida, USA (Apr. 30, 2009) pp. 1–10.
22. S. Scherer, S. Singh, L. Chamberlain and M. Elgersma, "Flying fast and low among obstacles: Methodology and experiments," *Int. J. Robot. Res.* **27**(5), 549–574 (2008).
23. B. Call, B. R. Randy, T. C. Clark, "Obstacle Avoidance For Unmanned Air Vehicles Using Image Feature Tracking," *Proceedings of AIAA Guidance, Navigation, and Control Conference and Exhibit*, Keystone, USA (Aug. 21–24, 2006) (chapter AIAA 2006-6541).

https://doi.org/10.1017/S0263574714001404 Published online by Cambridge University Press